ADVANCED FUNCTIONAL MATERIALS
www.afm-journal.de

Metal Oxide/Polymer Hybrid Nanoparticles with Versatile Functionality Prepared by Controlled Surface Crystallization

Viktor Fischer, Ingo Lieberwirth, Gerhard Jakob, Katharina Landfester, and Rafael Muñoz-Espí**

Metal oxide/polymer hybrids are prepared from polystyrene nanoparticles functionalized at the surface with phosphonate and phosphate groups. The polymer particles are synthesized with specifically designed surface-active monomers (surfmers) and used as nucleation surfaces for the controlled in situ crystallization of cerium, iron, and zinc oxide nanocrystals. The formation of the metal oxide is driven by the addition of a base to suspensions of the polymer particles containing the corresponding precursor. The crystal formation at the particle surface is studied for the different hybrid systems by X-ray diffraction and transmission electron microscopy (TEM). The potential catalytic activity of CeO_2/polymer hybrid particles is proven with the example of the photodegradation of rhodamine B. For the case of magnetic iron oxide-functionalized latex, a superparamagnetic behavior is found above a blocking temperature of 225 K. ZnO/polymer hybrids present a strong yellow visible photoluminescence. The approach is shown to be versatile not only in terms of the variety in the metal oxides deposited on the surface, but also because the crystallization can take place in both aqueous and alcoholic media.

1. Introduction

The controlled preparation of hybrid nanoparticles with defined functionality is nowadays an attractive task in materials science, because they have a broad scope of applications, including medicine,[1,2] catalysis,[3] molecular imprinting,[4] coatings,[5] and imaging.[6] Hybrid particles with inorganic components can be divided into inorganic–inorganic and organic–inorganic hybrid materials. For the preparation of inorganic–inorganic hybrids, silica is often applied as a core/template/carrier[7,8] or as a shell[9,10] material. For organic–inorganic hybrid particles, polymers may serve as carrier particles,[11] coating materials,[12] templates and structure-directing agents,[13–15] or to embed the inorganic component.[16] The application of polymer carrier particles has the easy processability as a significant advantage. The polymer can also be removed by dissolution[17] or calcination.[18]

Here, we focus on the generation of polymer/inorganic hybrids by the formation of metal oxide nanocrystals at the surface of functionalized latex particles. On account of a high variety of material properties and their fairly easy formation, metal oxides are especially suited candidates for the design of hybrid materials. The modification of polymer particles with metal oxide nanocrystals can indeed be applied to prepare materials with unique properties. Magnetic iron oxides, which have drawn for years the attention of many research groups,[19–22] are used to produce composites sensitive to magnetic stimuli for magnetic resonance imaging,[23] magnetoresponsive release applications,[24] and for an easier sample treatment.[25,26] Zinc oxide, one the most prominent semiconducting metal oxides,[27–29] has been especially studied for the preparation of luminescent materials[30] and quantum dots.[31,32] Rare metal oxides are used in some technically important applications, such as oxidation catalysis, being cerium(IV) oxide (ceria) one of the most representative examples.[33,34]

The specific arrangement of functional groups on the surface of polymer particles can provide nucleation and structure-directing centers for controlled crystallization from solution, which can be used to grow in situ the desired inorganic material. Functionalized polystyrene beads prepared by different emulsion techniques, including miniemulsion, have been previously used as a supporting material of different inorganic materials. Calcium phosphate and hydroxyapatite have been formed on the surface of polystyrene particles functionalized with poly(acrylic acid)[35,36] and poly(acetoxyethyl methacrylate).[37] Noble metal nanoparticles have also been often deposited on the surface of polystyrene beads with grafted polyelectrolyte brushes, being especially remarkable the achievements of Ballauff and coworkers.[38–40] In contrast to calcium phosphate and metals, the controlled crystallization of metal oxides on polymer spheres appears to be more complex. Poly(styrene-*co*-acetoxyethyl methacrylate), prepared in the presence of potassium persulfate (KPS) as an initiator, were used as carriers of in situ prepared ZnO,[41] TiO_2,[42] Ta_2O_5,[43] and $In(OH)_3$.[44] TiO_2 was also grown on the surface of polystyrene beads with long chains of poly(styrene sodium sulfonate).[45,46]

V. Fischer, Dr. I. Lieberwirth, Prof. K. Landfester,
Dr. R. Muñoz-Espí
Max Planck Institute for Polymer Research
Ackermannweg 10, 55128 Mainz, Germany
E-mail: landfester@mpip-mainz.mpg.de;
munoz@mpip-maiz.mpg.de
Prof. G. Jakob
Institute of Physics
University of Mainz
Staudingerweg 7, 55128 Mainz, Germany

DOI: 10.1002/adfm.201201839

In most of the previous cases, the presence of sulfate groups on the corona, resulting either from the use of KPS as an initiator or from sulfate-containing surfactants, may represent a drawback not only for the proper determination of the concentration of functional groups, but also because sulfate can influence the metal oxide formation, as discussed later on in this article. In case of particles prepared in the presence of surfactants, the purification by long dialysis and surfactant-exchange procedures (electrostatic/steric stabilization) makes sample handling and preparation tedious and difficult. Furthermore, it is important to note that the work reported so far for metal oxides involves crystallization from alcoholic solvents and not from aqueous media, which limits the applicability to a number of systems and crystal phases. Water-based systems are not only attractive from an environmental point of view, but they make also possible a straight forward processability and permit to use the prepared dispersions without any additional exchange of solvent.

In this work, we used surface-active monomers (so-called surfmers) to avoid the influence of a surfactant on the crystallization process and to assure that a non-hairy structure of functional groups is covalently attached to the surface of the particle. Polymer nanoparticles have been successfully prepared with phosphonate-functionalized[47] and carboxyl-functionalized[48] surfmers. The application of surfmers implies also an easy and simple dispersion purification and sample treatment. Exemplified for cerium, iron, and zinc oxides, we present a versatile approach to crystallize inorganic metal oxides on the surface of polymer nanoparticles. By our method, hybrid particles containing oxides with diverse properties (magnetic, optical, and catalytic properties) can be formed from both aqueous and alcoholic media, which increases the number of systems that can be prepared. We also provide an insight in the understanding of the procedure of metal oxide crystallization at functional surfaces.

2. Results and Discussion

The aim of this work was the design of colloidally stable polymer/inorganic hybrid nanoparticles comprised of a polymeric core and a metal oxide corona, formed in situ on the functionalized polymer surface. The polymeric particles were obtained by miniemulsion copolymerization of styrene with a surface-active functional comonomer (surfmer), which contains a phosphonate or a phosphate moiety and is able to act simultaneously as a surfactant and as a monomer. The phosphonate and phosphate surfmers were specifically synthesized to increase the colloidal quality by incorporating the surfactant in the particle shell during the miniemulsion polymerization process. The metal oxide formation occurred at the surface of the functionalized latex particles by mixing an aliquot of the latex dispersion with the metal oxide precursor solution. After a sufficient complexation time (see the Experimental Section) of the precursor, the crystallization was induced by addition of a precipitating agent (a base) at a certain dropping rate. This rate is crucial to control the supersaturation level and drive effectively the crystallization to the particle surface.

2.1. Synthesis and Characterization of Surface-Functionalized Latex Particles

The surfmers, which contain a methacrylate polymerizable group and the hydrophilic phosphonate or phosphate functionality, were synthesized by the three-step reactions presented in **Scheme 1**. The first step of the synthesis of the phosphonate surfmer was a base-catalyzed Schotten–Baumann reaction of methacryloyl chloride with 11-bromo-1-undecanol to give compound **1**, followed by a Michaelis–Arbuzov reaction leading to the ethyl-protected surfmer (**2**). Deprotection with trimethylsilyl bromide (TMSBr) followed by methanol addition yielded the desired surfmer (**3**), referred to in the following as RPO_3H_2 for the sake of clarity. In the case of the phosphate surfmer, a Schotten–Baumann reaction of diethyl phosphoryl chloride was carried out to obtain the protected functionalization at the undecane spacer (**4**). The polymerizable group was coupled to compound **4** with a phase-transfer catalyst (Aliquat 336), resulting in the ethyl-protected phosphate surfmer (**5**). The deprotection of compound **5** was achieved by adding consecutively TMSBr and methanol, which yielded the phosphate-functionalized surfmer (**6**), referred to further on as RPO_4H_2.

We synthesized three kind of functionalized latex particles to compare the influence of the functional group on the metal oxide formation: particles containing i) phosphonate, ii) phosphate, and iii) sulfate functionalities covalently bound to the particle surface. Phosphonate- and phosphate-functionalized particles were prepared by using small amounts of the

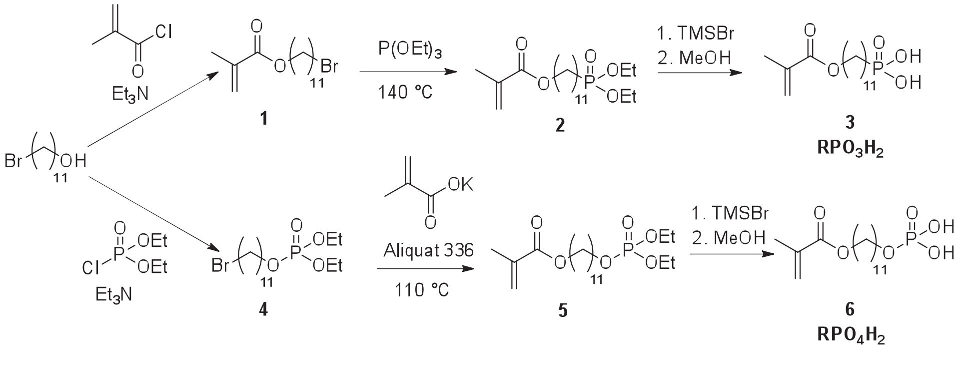

Scheme 1. Synthesis of phosphonate- and phosphate-functionalized surfmers.

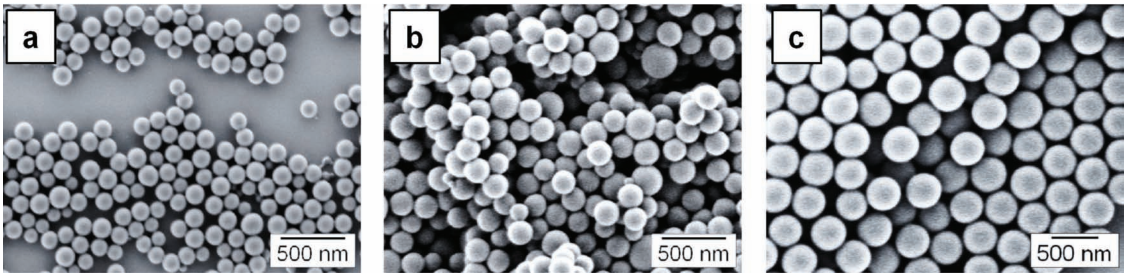

Figure 1. SEM images of functionalized latex particles prepared a) with the phosphonate surfmer, b) with the phosphate surfmer, and c) with the sulfate initiatior KPS (otherwise surfactant free).

previously synthesized surfmers in a miniemulsion copolymerization process with styrene. For sulfate-functionalized particles, we used a modified surfactant-free miniemulsion method. Since the surfactant is formed in situ, a prompt addition of potassium persulfate (KPS) dissolved in water and a preheated reaction vessel are crucial to obtain particles with a narrow size distribution. **Figure 1** presents SEM images of the latex particles synthesized with RPO_3H_2, RPO_4H_2, and KPS. The main characteristics of the synthesized samples are shown in **Table 1**. The solid contents of all latex dispersions are comparable and of a reasonable yield (12–17 wt%). The surface charge density changes drastically from pH 7.5 to 10 for phosphonate and phosphate particles, which is easily explained by the strong pH dependency of phosphonic and phosphoric acid. A full deprotonation can be only reached at basic pH values (pK_{a1} = 2.00, pK_{a2} = 6.59 for phosphonic acid,[49] and pK_{a1} = 2.16, pK_{a2} = 7.21, pK_{a3} = 12.23 for phosphoric acid;[50] pK_{a1} is negligible, since the most acidic OH– groups have reacted during the phosphoric ester formation of the surfmer). As sulfate does not show a pH dependency in the investigated range (pH 7.5 to 10), the surface charge stays constant.

To investigate the pH stability of the phosphate groups, we incubated the particle dispersion at different pH values (3, 7 and 12) for 48 h. Dark-field transmission electron microscopy and phosphor mapping showed that phosphor is present on the particle surface under all pH conditions (Figure S1, Supporting Information).

2.2. Crystallization of Metal Oxides on the Surface of Functionalized Latex Particles

The general procedure for the formation of metal oxides at the interface, which results in colloidally stable hybrid latex dispersions, is depicted in **Figure 2**. The metal oxide formation consists of two steps. In step I, the metal oxide precursor is added to the latex dispersion for complexation of the metal ions to the functional groups. For all metal ions, the dispersion collapsed and became unstable after complete precursor addition. To prove that the metal ions are complexed by the functional groups, we centrifuged the dispersions after the complexation step (step I) and determined the elemental composition of the supernatant by inductively coupled plasma–optical emission spectrometry (ICP–OES). A high complexation efficiency of ≥99.9% (see the last column of **Table 2**) demonstrates the complexation of the precursor ions. In step II, after gentle stirring and sufficient complexation time, the precipitating agent was added at a controlled rate. The dispersions were stirred for 24 h after finishing the base addition to ensure the complete crystallization of the metal oxide. All obtained hybrid latex dispersions were observed to be stable again.

To verify that the nucleation occurs actually at the particle surface and that the metal oxide nanoparticles are not formed in the solution and merely adsorbed or heterocoagulated on the polymer surface, we conducted control experiments by mixing metal oxide nanoparticles formed ex situ with the latex dispersions (see Experimental Section and Figures S2–S3 in the Supporting Information). After the blending of the polymers and the inorganic nanoparticles, the reaction conditions of the in situ experiments were adjusted by addition of the appropriate base and the application of the appropriate solvent (methanol or water). An adsorption or a heterogeneous coagulation of the inorganic component on the surface could not be observed (Figure S3, Supporting Information), which is a strong indication of the nucleation and in situ formation of the metal oxides at the surface of the functionalized latex particles.

The versatility of the approach was investigated by preparing hybrid particles containing different metal oxides, including cerium, iron, and zinc oxides. **Figure 3** shows SEM images of hybrid latex obtained from aqueous solutions of Ce(IV), Fe(III),

Table 1. Characteristics of the latex dispersions prepared with phosphonate (RPO_3H_2) and phosphate (RPO_4H_2) surfmers, and with potassium persulfate (KPS).

	Solid content [wt%]	Particle size [nm]	Surface charge density [nm^{-2}]		Number of functional groups	
			pH = 7.4	pH = 10.0	[nm^{-2}]	[$\times 10^4$ per particle]
RPO_3H_2	12.6	143 ± 17	0.18	0.63	0.31	2.01
RPO_4H_2	16.4	198 ± 14	0.26	0.82	0.41	5.03
KPS	14.8	390 ± 57	0.73	0.79	0.79	37.5

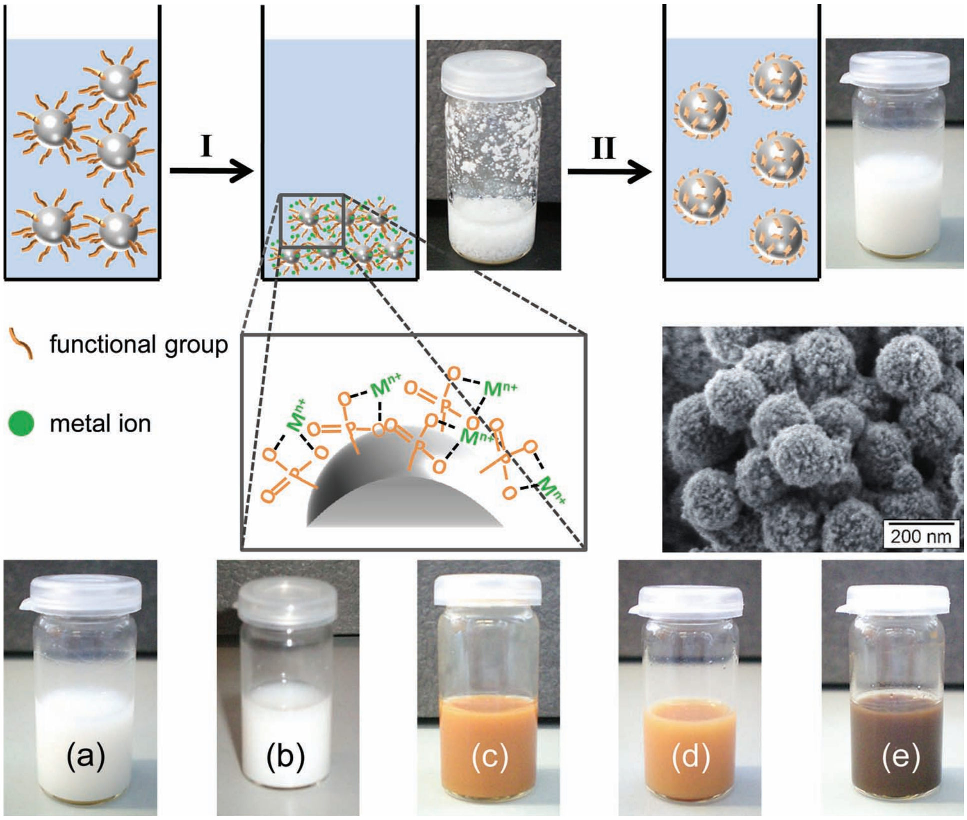

Figure 2. Mechanism of metal oxide formation at the surface of phosphonate- or phosphate-functionalized particles. At the bottom, colloidally stable dispersions of different hybrid particles are shown: a) CeO_2 from H_2O, b) ZnO from MeOH, c) Fe_2O_3 from H_2O, d) Fe_2O_3 from 2-propanol, and e) Fe_3O_4 from H_2O. The embedded image shows ceria formed at the surface of phosphate-functionalized particles.

and Fe(II) for both phosphonate- and phosphate-functionalized particles. The particles are efficiently covered with the corresponding metal oxides. For CeO_2, a dense and homogeneous particle coverage is seen. Fe_2O_3 (obtained from Fe(III) solutions) and Fe_3O_4 (obtained from Fe(II) solutions) show a lower surface coverage and a more "raspberry-like" structure. Further

Table 2. Measured zeta potential (ζ), surface area (determined by BET), crystallite sizes (L) estimated from PXRD, metal oxide content (c_{MO}), and complexation efficiency for hybrid particles prepared with the phosphate and phosphonate surfmers from different solvents.

Solvent	Metal oxide	Surfmer	ζ [mV]	Surface area [$m^2\ g^{-1}$]	L_{av} [nm]$^{a)}$	c_{MO} [wt%]$^{b)}$	Complexation efficiency [%]$^{e)}$
H_2O	particles	RPO_3H_2	−55 ± 8	21	–	–	–
		RPO_4H_2	−57 ± 6	19	–	–	–
	CeO_2	RPO_3H_2	25 ± 3	48	3.3 ± 0.1	33.5	99.91
		RPO_4H_2	27 ± 6	47	3.0 ± 0.1	34.2	99.91
	$Fe_2O_3$$^{d)}$	RPO_3H_2	−41 ± 5	42	1.5 ± 0.1$^{c)}$	28.3	99.96
		RPO_4H_2	−38 ± 4	45	1.2 ± 0.1$^{c)}$	25.0	99.96
	Fe_3O_4	RPO_3H_2	−46 ± 5	45	10.1 ± 0.3	29.9	99.96
		RPO_4H_2	−49 ± 4	46	10.0 ± 0.4	23.9	99.95
MeOH	ZnO	RPO_3H_2	−13 ± 5	84	11.0 ± 0.5	37.3	99.93
		RPO_4H_2	−16 ± 8	72	9.7 ± 0.2	30.4	99.94
2-propanol	$Fe_2O_3$$^{d)}$	RPO_3H_2	38 ± 7	72	2.3 ± 0.3$^{c)}$	22.7	99.96
		RPO_4H_2	40 ± 6	67	2.1 ± 0.1$^{c)}$	23.7	99.96

[a)] Average crystallite sizes resulting from averaging the size determined from the width of the two PXRD reflections with highest intensity, unless stated otherwise; [b)] Metal oxide content (c_{MO}) determined from the weight loss by TGA measurements under N_2 atmosphere; [c)] Determined from TEM images (the error corresponds to the standard deviation of the measured planes); [d)] Iron oxide formed from Fe(III) precursor was found to be Fe_2O_3 (hematite) after calcination; [e)] Determined by ICP-OES.

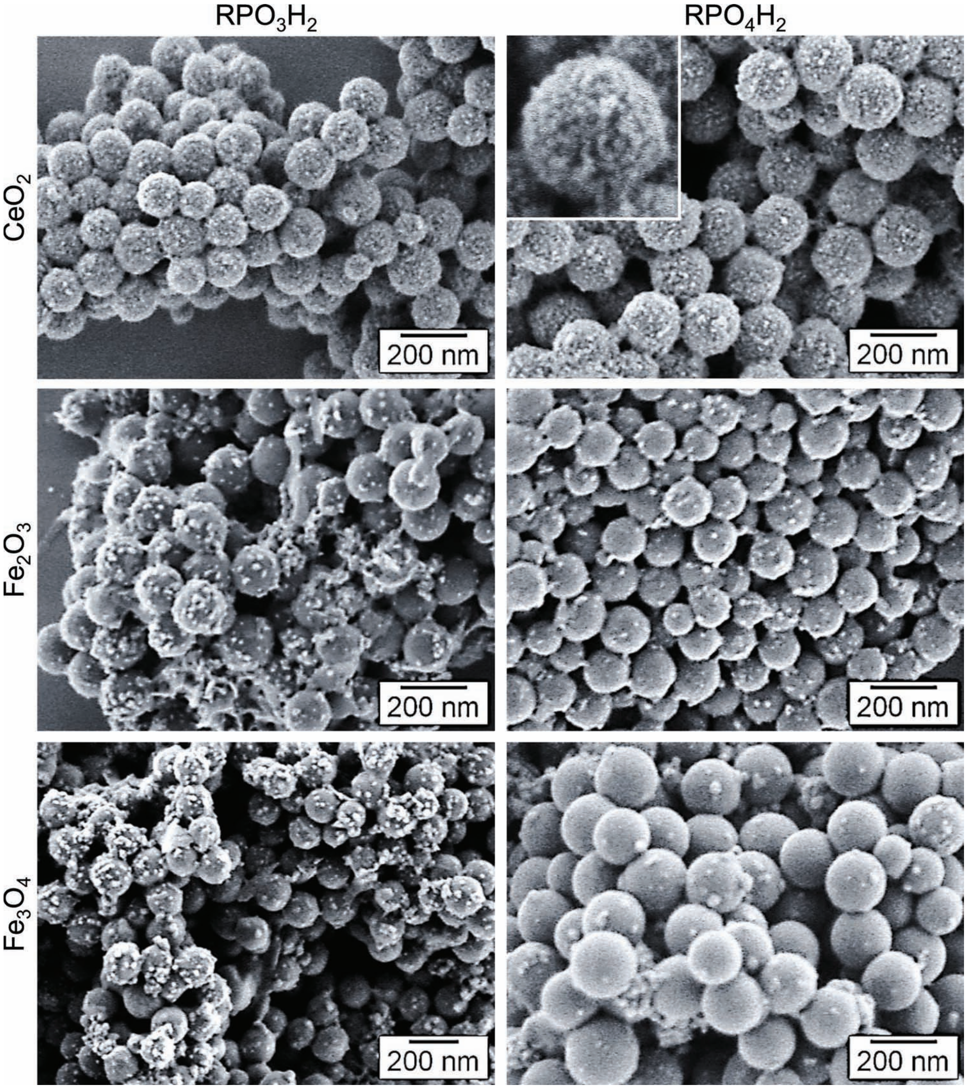

Figure 3. SEM images of metal oxide/polymer hybrid particles prepared with phosphonate- and phosphate-functionalized latex particles in aqueous dispersions.

experiments were carried out in methanol, ethanol, and 2-propanol to explore the extension of the method to non-aqueous solvents. SEM images of some representative cases are shown in **Figure 4**. The iron(III) oxide hybrid particles obtained from 2-propanol presented a more dense coverage than those formed from aqueous solution, which can be explained by the sol–gel-like oxide formation of iron oxide in alcoholic solvents.[51] ZnO could not be prepared from aqueous solution, as discussed below, but a raspberry-like particle coverage could be achieved from methanol or other alcoholic solvents (i.e., ethanol and 2-propanol, Figure S4 in the Supporting Information).

As small metal oxide nanoparticles are attached to the surface of the polymer beads, we assume that a "Pickering-like" mechanism is responsible for the stabilization of the hybrid colloids. As seen in **Figure 5**a, the value of the zeta potential (ζ) increases after the formation of the metal oxide, which indicates that the electrochemical surrounding of the particle is changing. We postulate that the stabilization of the particles correlates with the zeta potential of the metal oxide formed at the surface and the remaining functionalized groups. A model for the stabilization of the particles is shown in Figure 5b. The metal oxide crystals formed at the particle surface are terminated by negatively charged O^- species. This negative charge is compensated by a small excess of cations provided by the precipitating agent. The zeta potential $\zeta^{\pm}_{\text{total}}$ of the hybrid particles could be then described by:

$$\zeta^{\pm}_{\text{total}} = \zeta^{-}_{\text{blank}} + \zeta^{+}_{\text{MO}} \tag{1}$$

This means that the measured zeta potential is composed by the contribution of the unloaded particles (ζ^{-}_{blank}) and the contribution of the metal oxide at the surface (ζ^{+}_{MO}). For full particle coverage, the term ζ^{-}_{blank} does not contribute to the total zeta potential value, because the functional groups are shielded by the metal oxide and do not interact with the ions in solution. Sodium (for the case of CeO_2) and potassium (for the case of

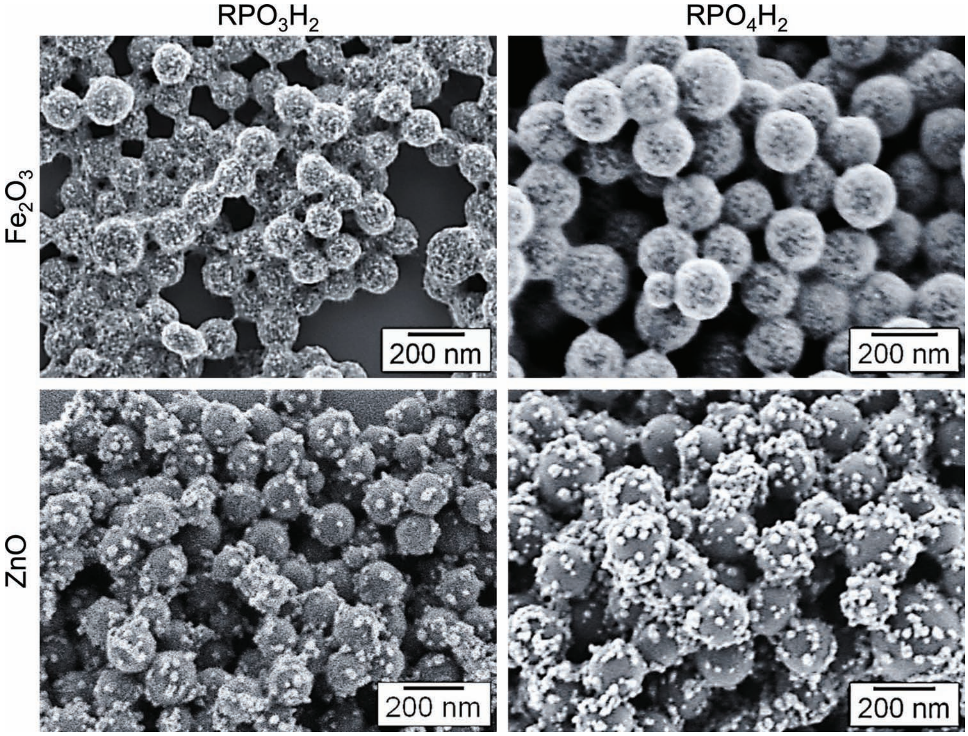

Figure 4. SEM images of metal oxide/polymer hybrid particles prepared with phosphonate- and phosphate-functionalized latex particles in alcoholic dispersions (2-propanol for the case of the Fe_2O_3 and methanol for the case of ZnO).

ZnO) are part of the Stern layer of metal oxide nanoparticles formed on the latex surface, which is in agreement to that proposed by Ozin et al.[5] for pure metal oxide particles. Elemental analysis by energy-dispersive X-ray (EDX) spectroscopy confirmed the presence of sodium and potassium in the investigated areas (Figures S5–S6, Supporting Information). Although EDX analysis could not be performed for iron oxide hybrid particles (NH_4^+ cannot be detected by this method), the change in zeta potential is supporting the postulated "positively charged" crystals. In contrast to all other experiments, iron oxide precipitated from 2-propanol is formed in an acidic medium, which results from the acid behavior of the formed iron hexa-aquo complexes:

$$Fe[(H_2O)_6]^{3+} \rightleftarrows [Fe(OH)(H_2O)_5]^{2+} + H^+ \quad (2)$$

Therefore, the surface of the iron oxide crystals is terminated by positively charged groups ($=OH^+$ or $-OH_2^+$), which together with adsorbed hydrogen ions form the Stern layer, as also reported by Ozin et al. for pure iron oxide particles formed in alcoholic solvent.[5] According to this model, we can also conclude that the increase of zeta potential correlates with the surface coverage of the latex particles.

Besides phosphonate- and phosphate-functionalized latexes, the influence of the functional groups on the metal oxide formation was further investigated with sulfate-functionalized particles. The precipitation of the oxides on the sulfate particles was conducted analogously to the procedure used for the phosphonate and phosphate ones. In contrast to phosphonate and phosphate particles, only ceria could be efficiently formed at the surface of sulfate-functionalized particles, and bulk crystallization occurred for zinc and iron oxides (Figure S7, Supporting Information). This behavior indicates that the nature of the functional group is important for the formation of the metal oxide. Iron, cerium, and zinc phosphates are very soluble in water. Differently, the corresponding sulfates are poorly water soluble, with the exception of cerium sulfate, which is also slightly soluble in water. Considering the solubility of the phosphates and sulfates, we postulate that the complexation strength, and, thus, the ability of functional groups to immobilize the metal precursor ions at the particle surface, correlates to the "hardness" of the corresponding bases according to the "hard and soft acids and bases" (HSAB) concept. For the case of the formation of iron and zinc oxide with the described process, the sulfate-functionalized particles loaded with metal ions serve as reservoir of the metal ions to the crystals growing in bulk.

To investigate the influence of the addition rate of the precipitating agent, ceria was precipitated by adding NaOH at different addition rates in the presence of RPO_3H_2-functionalized latex particles. Prompt addition leads to bulk crystallization of small ceria particles. Also a base addition with rates of 4 and 8 mL h^{-1} led to the formation of big bulk crystals and not to small ceria particles at the surface (Figure S8, Supporting Information). We assume that if the supersaturation level of cerium hydroxide species raises too fast, the latex particles are not serving as nucleation centers for heterogeneous nucleation and mainly bulk crystallization occurs.

Powder X-ray diffraction (PXRD) patterns of hybrid samples prepared with phosphonate and phosphate particles are presented in **Figure 6**. Reflections of samples prepared from

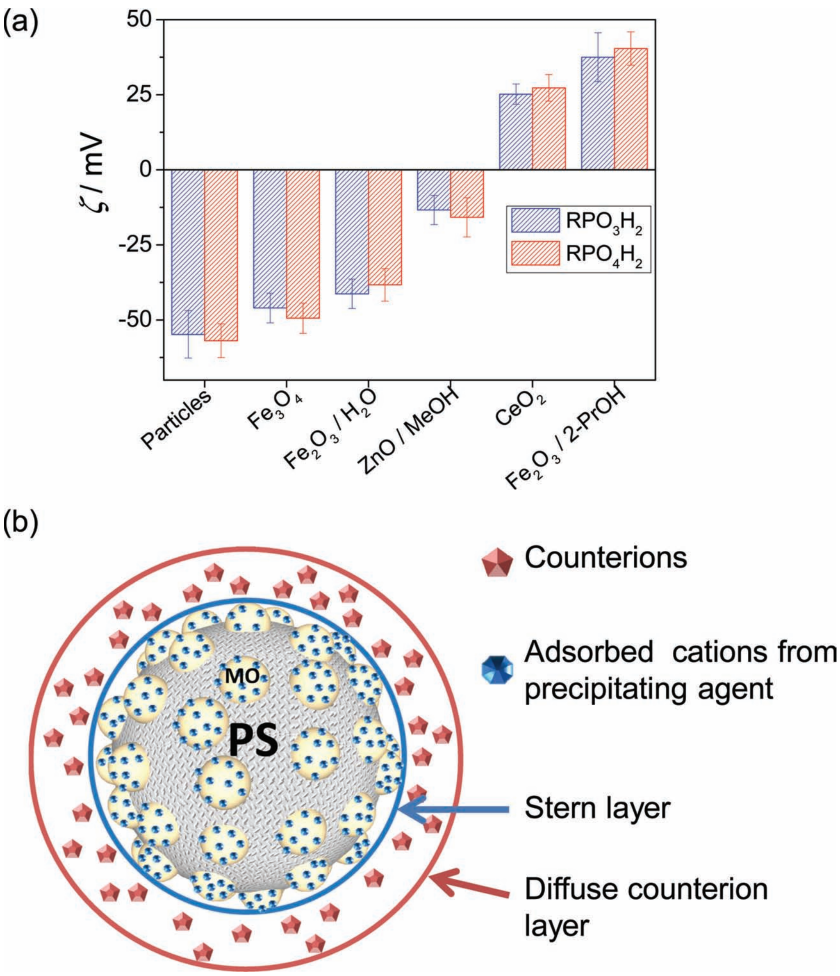

Figure 5. a) Measurements of the zeta potential (ζ) for metal oxide hybrids prepared with phosphonate- and phosphate-functionalized PS particles. b) Stabilization mechanism of hybrid latex in dispersion.

cerium precursors correspond to crystalline CeO_2 (ceria, JCPDS card No. 34-0394). Iron oxide samples prepared from Fe(II) aqueous solutions could be identified as Fe_3O_4 (magnetite, JCPDS card No. 19-629), although the formation of magnetic γ-Fe_2O_3 (maghemite) cannot be excluded by our analytic methods. All iron oxide hybrid particles prepared from a Fe(III) precursor, with independence of the solvents used, appear to be amorphous according to the PXRD patterns. After calcination, all samples transform to α-Fe_2O_3 (hematite, Figures S9–S10, Supporting Information). Zinc oxide (zincite, JCPDS card No. 36–1451) was found to form from methanolic solutions on both phosphonate and phosphate particles. In the phosphonate-containing samples, however, two additional reflections could not be unambiguously assigned to any known crystal phase, but are temptatively assigned to zinc hydroxide species. The thermogravimetric analysis (TGA) trace of this sample showed a sharp peak of the first derivative at 130 °C with a weight loss of 3.4 wt%, which is consistent with the assumption of hydroxide species (Figure S9, Supporting Information). As expected, only ZnO could be identified after calcination in the PXRD patterns (Figure S10, Supporting Information). Under the used conditions (room temperature and ambient pressure), ZnO could not be formed from aqueous solutions. The zinc compound formed on the phosphonate- or phosphate-functionalized particles appears as long needles covering the particle (Figure S11, Supporting Information). The corresponding PXRD patterns could not be assigned to any known reference compound (Figure S12, Supporting Information). As zinc phosphate has a lower solubility than zinc hydroxide, we assume that the phase formed at the surface may be a zinc hydroxide phase.

Average crystallite sizes (L_{av}), reported in Table 2, were calculated as the average of the sizes obtained by the Scherrer equation from the width of the two PXRD reflections with the highest intensity (L_{hkl} values in the Supporting Information, Table S1). Sizes of the nanocrystals formed at the surface of the polymer particles are in the range of ca. 3–10 nm.

TEM images of ceria hybrid latex (RPO_3H_2 and RPO_4H_2), presented in **Figure 7**, show a homogeneous distribution of ceria nanocrystals on the particle surface. The presence of bright spots on the dark-field images (Figure 7b) confirm crystalline domains lying in the detection plane. The positive zeta potential value of ceria hybrid particles supports these microscopical observations. Electron diffraction patterns show that the formed ceria is of polycrystalline nature, coinciding with the results from PXRD. For the Fe_3O_4-containing hybrid particles (i.e., iron oxide samples prepared from a Fe(II) solution), crystalline domains corresponding to the crystallite sizes calculated by PXRD, are grown at the particle surface (Figure S13, Supporting Information). According to the images, after complexation and nucleation of Fe_3O_4, the crystal growth seems to occur orthogonal to the particle surface, forming bigger crystals than for the case of ceria. This leads to non-fully covered particles. Consistently, the negative value of the zeta potential suggests that many surface functional groups are not covered by the iron oxide nanocrystals. TEM images of the ZnO hybrid particles show a “raspberry-like” coverage with crystalline domains of around 9 nm (Figures S14–S15, Supporting Information), which coincides with the estimations by the Scherrer equation from PXRD. The coverage of the particles by ZnO nanocrystals is higher than for Fe_3O_4, which is also confirmed by a higher value of the zeta potential. The crystal growth for ZnO occurs similar to Fe_3O_4 and the high-resolution images indicate that the nanocrystals grow orthogonal to the surface of the polymer particle.

Although the electron diffraction patterns of iron oxide samples prepared from iron(III) precursors indicate an overall amorphicity of the metal oxide formed, TEM dark-field images shown in **Figure 8** proved that small crystallites are present at the particle surface. The variation of the detection angle

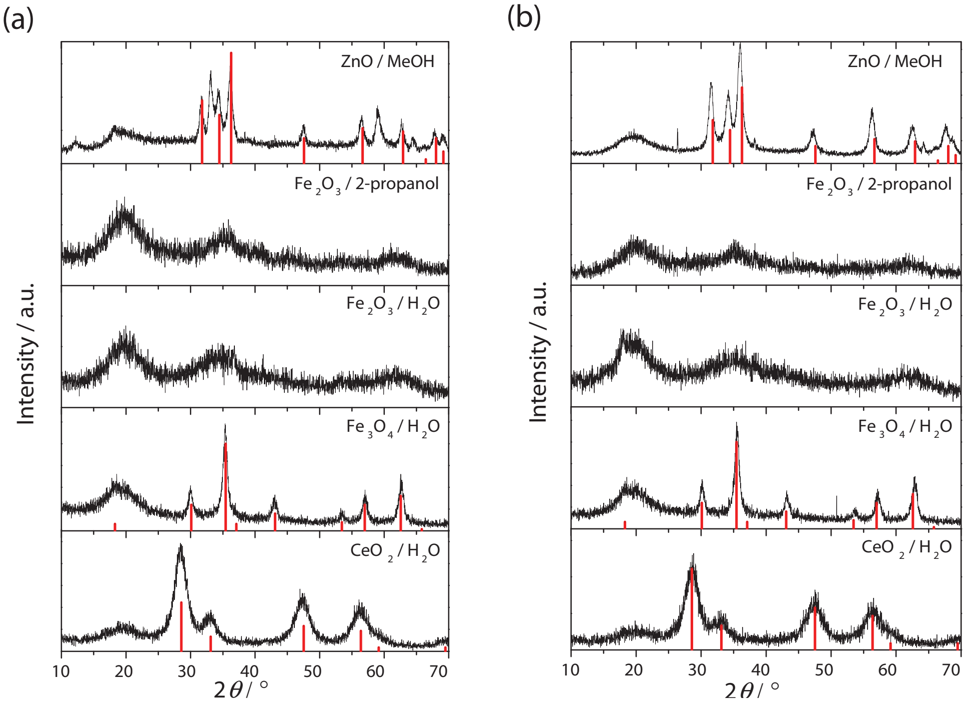

Figure 6. PXRD patterns of metal oxides prepared with a) phosphonate-functionalized and (b) phosphate-functionalized particles. Vertical lines indicate the position and relative intensity of known metal oxide crystal phases: CeO_2 (JCPDS card No. 34-0394), Fe_3O_4 (JCPDS card No. 19-0629), ZnO (JCPDS card No. 36-1451).

(cf. panels b,c in Figure 8) revealed further crystallites with a different alignment of their lattice with respect to the surface. Small crystalline domains were observed in high-resolution images (Figure 8d and Figures S18–S19, Supporting Information). Interplanar distances of 2.5 Å and 2.7 Å can be obtained from the images, which correspond to the planes (104) and (110) of hematite. Elemental mapping by EDX confirmed the distribution of iron and oxygen at the surface of the polymer particles (Figures S16–S17, Supporting Information). Neither the functionality of the latex particles (phosphonate or phosphate) nor the used solvent (water or 2-propanol) seem to have an influence on the formation of crystalline domains (see also Figures S18–S20, Supporting Information). We conclude, therefore, that amorphous hematite was formed at the particle surface and "trapped" in a state right before crystallization. The amorphous iron oxide represents a post-critical nucleation matrix and small crystalline domains can be seen as immobilized post-critical nucleation clusters or nuclei on which crystal growth can take place.[52,53]

The content of the metal oxide component in the hybrid particles, c_{MO}, was determined by TGA and was as high as 23–37 wt% (Figure S9, Supporting Information). The surface area of the hybrid particles was determined by nitrogen adsorption according to BET theory. Hybrid particles feature a high surface area ranging from 42 to 84 $m^2 g^{-1}$, as seen in the values contained in Table 2, which is at least twice the value of unloaded blank latex particles. It is remarkable that hybrid particles prepared from alcoholic solutions exhibit up to a factor of 2 higher surface area than analogous samples prepared from aqueous media. In contrast, the functional groups do not seem to have any influence on c_{MO} and the surface area.

2.3. Catalytic Properties of CeO_2/Polymer Hybrid Particles

A photocatalytic oxidation of rhodamine B was carried out to investigate the catalytic properties of CeO_2/polymer hybrid particles. For this purpose, a rhodamine B solution and the hybrid latex dispersion were mixed and irradiated with UV light at constant temperature. The advance of the reaction was followed by measuring the decrease of the fluorescence emission intensity of rhodamine B.

Figure 9a shows the PL emission spectra at different times for fractions of a sample containing rhodamine B and a defined amount (1.0 wt%) of the hybrid CeO_2/phosphonate particles (equivalent spectra for CeO_2/phosphate particles are shown in Figure S22, Supporting Information). The overall fluorescence intensity decreases until almost no emission is observed after 3 h. The evolution with time of the ratio between the measured (I_t) and the initial (I_0) intensities is presented in Figure 9b. It is clearly seen that the photooxidative degradation of rhodamine B is much faster in the presence of the hybrid particles than without catalyst. The curves can be fitted to an exponential decay, which implies a pseudo-first order kinetics:

$$\frac{I_t}{I_0} = A_0 e^{-kt} \qquad (3)$$

where k is the reaction rate and A_0 is a fitting constant. The kinetic constants resulting from the fittings are 2.86×10^{-2} and 4.36×10^{-2} min^{-1} for the CeO_2/phosphonate and CeO_2/phosphate hybrid particles, respectively. The reaction rate of the phosphate-containing particles is slightly higher that of

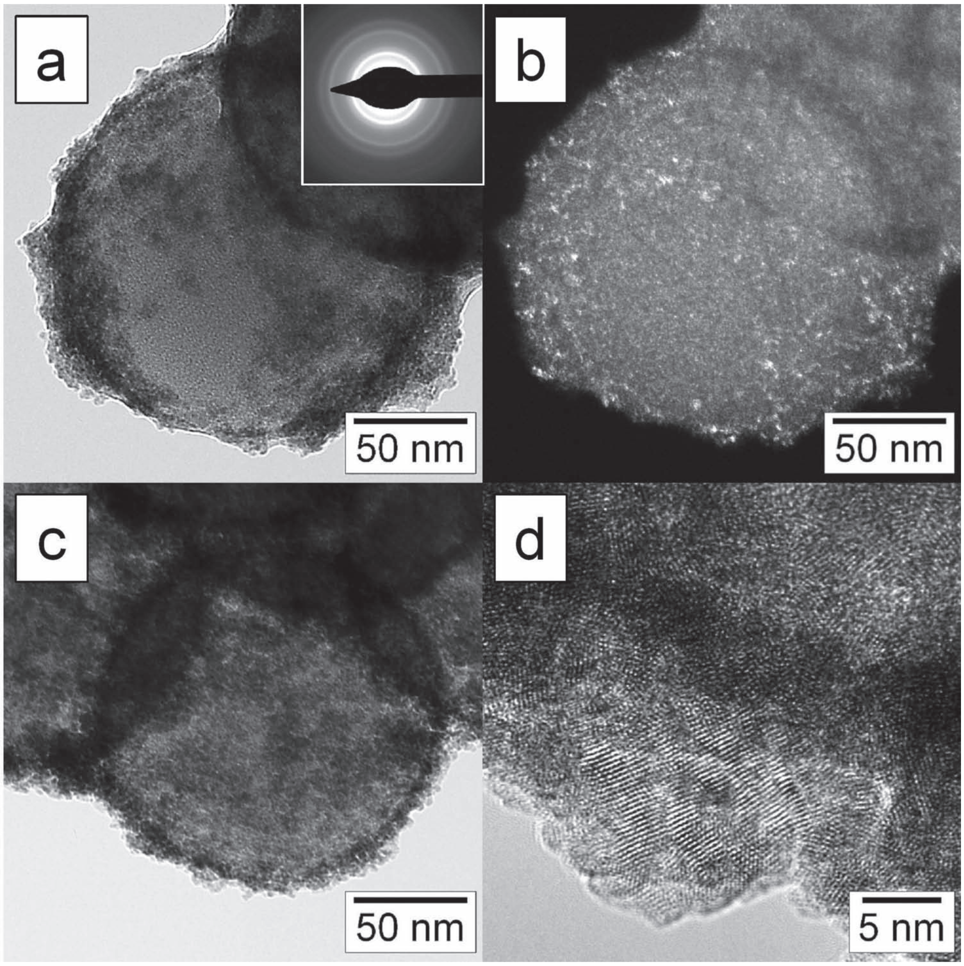

Figure 7. TEM images of CeO_2/polymer hybrid particles: a) bright-field image of a sample prepared with phosphonate-functionalized particles (inset shows the electron diffraction of the shown area) and b) corresponding dark-field image. c) Bright-field image of a sample prepared with phosphate-functionalized particles and d) corresponding high-resolution image.

phosphonate-containing ones, but in the same range. After 3 h, a degradation of the dye of 92% was achieved for both hybrid particle systems.

As a reference, we also carried out experiment using commercial cerium(IV) oxide powders. A concentration of at least 1 wt% of pure ceria powder was needed to see a catalytic effect. In comparison to the hybrid particles, the slope of the curve is less pronounced (Figure 9b). The rate constant from the curve fit was determined to be 1.59×10^{-3} min^{-1}, which is ten times smaller than for the hybrid particles. With respect to the ceria content of the hybrid particles, a 72% higher amount of ceria was needed to achieve a photocatalytic degradation.

2.4. Magnetic Properties of Fe_3O_4/Polymer Hybrid Particles

Magnetic properties of the produced Fe_3O_4/polymer hybrid particles were measured in a superconducting quantum interference device (SQUID) magnetometer in a field range of –40000 to 40000 Oe. Magnetization curves of a hybrid latex, presented in **Figure 10**, are reversible and do not show remanescence, coercivity or hysteresis in this field scale. Hybrid particles prepared with RPO_3H_2-functionalized latex show a slightly higher saturation magnetization (18.06 emu g^{-1}) than those prepared with the RPO_4H_2 latex (14.93 emu g^{-1}). To check the quality of the magnetic iron oxide formed at the interface, the curves in Figure 10a were correlated to the metal oxide content of the hybrid particles, c_{MO}, determined by thermogravimetry (cf. Table 2). After this correction, magnetic iron oxide at PO_4H_2-functionalized particles shows a slightly (62.49 emu g^{-1}) but not significantly higher magnetization than the one formed on RPO_3H_2-functionalized particles (60.97 emu g^{-1}). Bulk magnetite has typically a saturation magnetization of 92–100 emu g^{-1}, while the value for bulk maghemite is of 60–80 emu g^{-1}.[54] Since the crystal size and shape, as well as the additives used, have a high influence on the magnetization,[55] we cannot conclude whether magnetite or maghemite was formed. The measured magnetization behavior at room temperature (Figure 10b, symbols) is well described by that of superparamagnetic particles (green curve). The red curve in the inset of Figure 10b assumes monodisperse particles and is calculated from a scaled Brillouin function for superparamagnetic particles with

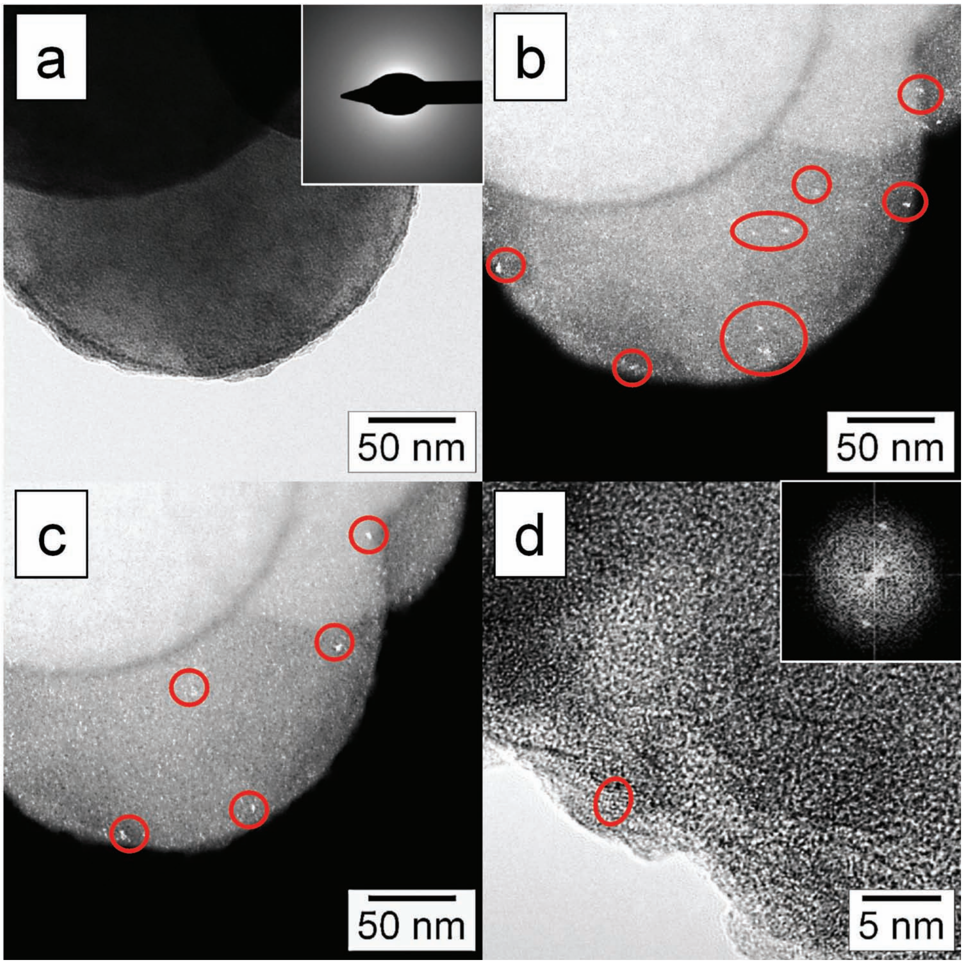

Figure 8. TEM images of iron oxide deposited on phosphate-functionalized particles obtained from 2-propanol: a) bright-field image and corresponding electron diffraction pattern (inset). b,c) Dark-field image of the same area shown in (a) at two different detecting angles. Bright signals indicating small crystallites are highlighted with red circles. d) Corresponding high-resolution image (inset shows Fourier transformation of the highlighted crystalline domain, $d = 2.7$ Å).

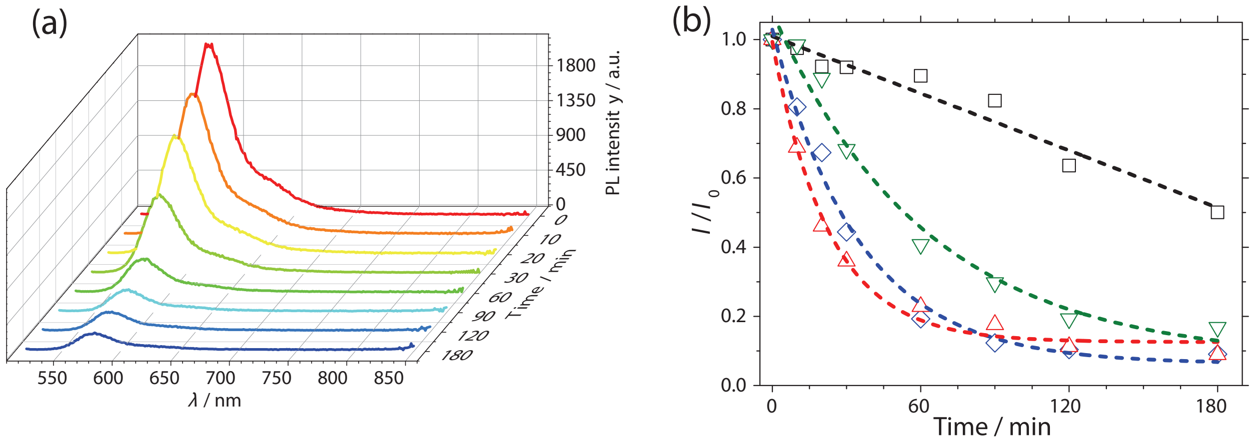

Figure 9. Photocatalytic degradation of rhodamine B: a) decrease of PL emission intensity over time in the presence of CeO_2/polymer hybrid particles prepared with phosphonate-functionalized latex. b) Decrease of maximum intensity at 580 nm normalized to the intensity at $t = 0$ for hybrid particles prepared with the phosphonate (blue) and phosphate (red) surfmers, compared to rhodamine B without any catalyst (black) and in the presence of commercial CeO_2 powder (green).

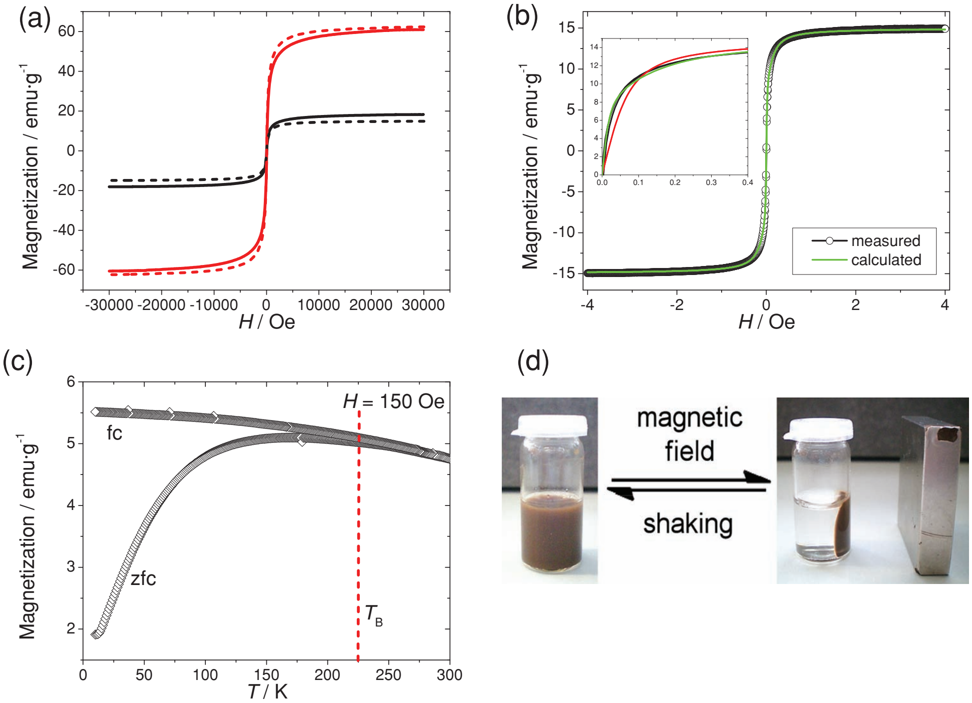

Figure 10. a) Magnetization measured at 300 K for Fe_3O_4/polymer particles prepared with phosphonate particles (black solid line) and phosphate particles (black dashed line); red lines show the magnetization with respect to the iron oxide content (determined by TGA). b) Measured magnetization for Fe_3O_4/polymer hybrids prepared with phosphate particles (symbols) plotted together with the calculated superparamagnetic behavior of monodisperse iron oxide particles (red curve) and for a bidisperse mixture of iron oxide particles (green curve). c) Temperature dependence of the magnetization of phosphate hybrid particles measured at a magnetic field of 150 Oe under zero field cooled (zfc) and field cooled (fc) conditions. d) Photograph of dispersed Fe_3O_4 composite latex under application of a magnetic field.

magnetic moments of 14800 Bohr magnetons, μ_B. The superparamagnetic magnetization for such monodisperse particles cannot describe the low-field behavior well. However, with a bimodal distribution of superparamagnetic particles with moments of 5000 μ_B and 60 000 μ_B in a mass ratio of 5:8, we calculated the green magnetization curve, which fits nicely to the data. Assuming 100 emu g^{-1} for the magnetization of Fe_3O_4, this translates to particles of radii with 2.8 nm and 6.4 nm and a total surface to mass area of 133 m^2 g^{-1}. As the magnetite particles have presumably a lower volume magnetization due to thermal fluctuations and reduced magnetization at the surface, the radii given above are lower limits, while the surface to mass ratio is an upper limit. Deviations from a perfect superparamagnetic behavior are obvious in the temperature-dependent measurements at a constant small field of 150 Oe (Figure 10c). The zero field measurement (zfc) deviates from the field cooled measurement (fc) at blocking temperatures around 225 K. For low temperatures, magnetocrystalline and shape anisotropies hinder a magnetic alignment in small fields. The photograph in Figure 10d shows how the Fe_3O_4/polymer hybrid colloid behaves when exposed to a magnetic field. Hybrid particles are moving to the vessel wall of the exposed side leaving a clear solution. The comparison of this behavior with the one shown by the sulfate-functionalized particles, in which the magnetite formation at the surface failed (Figure S21a, Supporting Information), is a further evidence that each particle is covered with magnetic iron oxide. Control experiments prepared by blending phosphonate functionalized particles and ex situ formed magnetite particles showed that only the magnetite could be separated by the presence of a strong magnet, but not the polymer particles (Figure S21c, Supporting Information).

2.5. Optical Properties of ZnO/Polymer Hybrid Particles

Photoluminescence (PL) emission and excitation spectra of hybrid ZnO/polymer hybrids are presented in **Figure 11**. The hybrid particles show a strong visible emission in the range 400–850 nm with a maximum in the yellow region at about 580 nm (2.14 eV) and 575 nm (2.16 eV) for RPO_3H_2 and RPO_4H_2 particles, respectively. ZnO on phosphate particles shows higher PL intensity than the analogous samples with phosphonate. This strong luminescence can also be simply observed by naked eyes under UV irradiation, as seen in the photograph of Figure 11c. Besides this visible emission both hybrid systems show a relatively narrow and small band at 389 nm (3.19 eV), assigned to the intrinsic emission of ZnO due to exciton recombination.[56,57] PL excitation spectra of both samples show a maximum peak at 350 nm (3.55 eV). The origin of the broad visible emission band may have different explanations and is heavily discussed in literature. The most common are residual copper impurities,[58] oxygen vacancies[59] and zinc vacancies acting as acceptor levels,[60,61] but it has been also attributed to trap-state emission due to surface defects,[30] surface hydroxides[62] or surface bonded molecules.[32] The visible emission was found

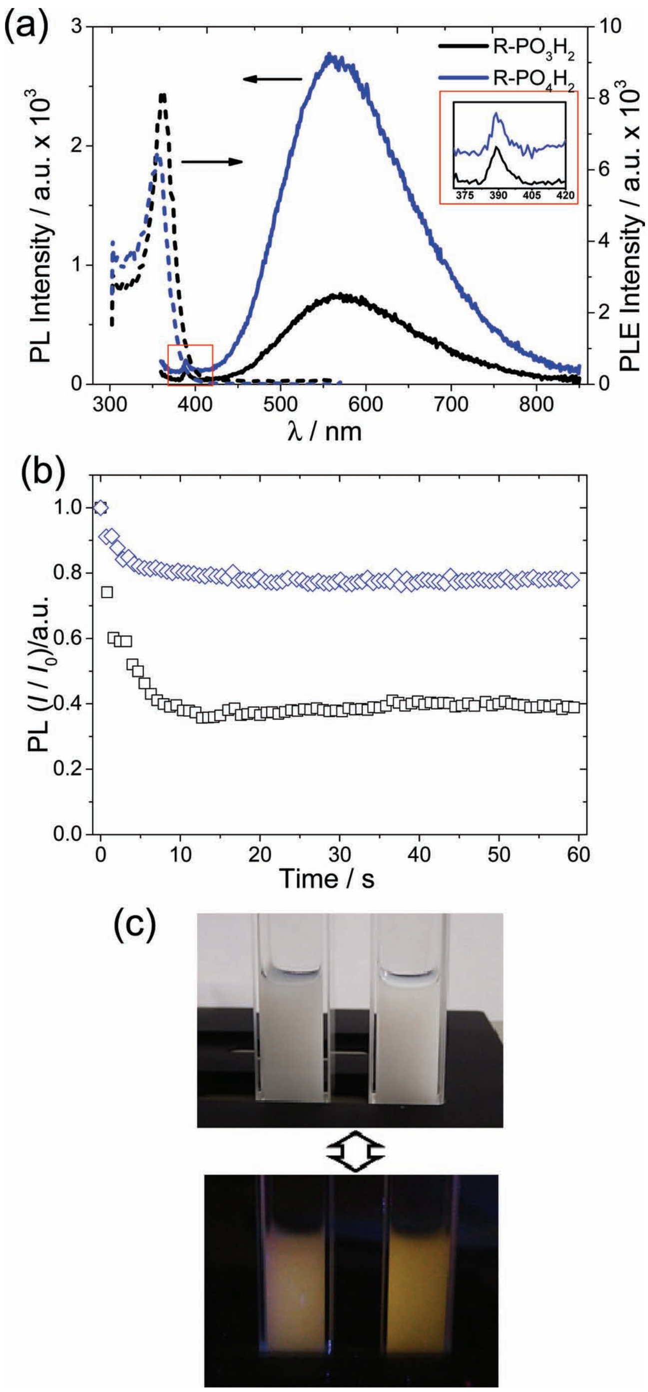

Figure 11. a) Photoluminescence emission spectra (excitation at 350 nm for black and blue curves) and photoluminescence excitation spectra (detection at 580 and 575 nm for black and blue curves, respectively) of ZnO/polymer hybrid particles. b) Dynamic behavior of the photoluminescence emission of ZnO hybrid particles (excitation at 350 nm, detection at 580 and 575 nm for black and blue curves, respectively). c) Photograph of ZnO/latex hybrid dispersions (left: RPO_3H_2, right: RPO_4H_2) under normal light and after UV light irradiation.

to present a dynamic behavior, as shown in Figure 11b: under constant irradiation, the photoluminescence intensity decreases until a plateau is reached. For RPO_4H_2 particles, the PL yellow emission decreases about 20% and for the RPO_3H_2 particles up to about 60%. Such kind of dynamic behavior has also been observed in previous work and was explained in terms of photodesorption of oxygen species contained in a depletion layer.[63] Oxygen has a strong tendency to adsorb to zinc oxide surfaces, acting as an electron acceptor. Adsorbed O_2 forms a negatively charged layer with low conductivity (depletion layer) by capturing electrons from the conduction band. If the ZnO nanoparticles are irradiated with UV light of an energy around the band gap (360 nm, 3.37 eV) photogenerated holes migrate to the negatively charged depletion layer in which the charged oxygen species are discharged. The discharged oxygen species desorbs more easily than O_2^- (photodesorption), leading to a degradation of the oxygen depletion layer. Thus, the depletion layer electrons can move freely and the conductivity increases. The O_2 desorption continues until an equilibrium between the adsorbed and the free species is achieved.[63] This is a simplified description of an adsorption/desorption procedure, but in a more realistic scenario adsorbed oxygen species of different oxidation states may react with crystal defects, generating more complex species.[64] The more significant decrease of the yellow emission for the case of RPO_3H_2-functionalized latex may be explained by the presence of hydroxide species that may quench the excitonic transitions.[65]

3. Conclusions

Phosphonate- and phosphate-containing surfmers were synthesized and applied for the preparation of functionalized latex particles with a narrow size distribution by miniemulsion polymerization. Those particles were used as polymeric carriers for the formation of metal oxide nanocrystals on their surface, which led to colloidally stable dispersions of the polymer/inorganic hybrid particles.

The versatility of the method was shown by preparing hybrid particles containing oxides of three different metals: cerium, iron, and zinc. Taken as a model case, the photodegradation of rhodamine B demonstrated that particles containing CeO_2 are effective as catalysts. A strong magnetization was found for the iron oxide/polymer hybrid particles, which presented a superparamagnetic behavior above a blocking temperature around 225 K. For the case of samples prepared from Fe(III) precursors, the investigation on crystal formation leads to the observation of immobilized post critical iron oxide nuclei at the particle surface. Particles with crystalline ZnO nanocrystals at the surface showed a very intense photoluminescence band in the yellow visible range (575–580 nm, 2.14–2.16 eV).

The chemistry of the complexating group on the surface was found to be crucial in the metal oxide formation. We could not observe a significant difference between particles prepared with phosphate and phosphonate, but mainly bulk crystallization occurred in the presence of sulfate groups. We propose a "Pickering-like" model for the stabilization of the hybrid particles in which the formed metal oxide nanoparticles act as stabilizers of the hybrid particles. The formation of crystalline metal oxides was successful in both aqueous and alcoholic media, which implies that the approach is not limited at the systems shown here, but it can be extended to a wide range of metal oxides.

4. Experimental Section

Materials: Reagents were purchased from Sigma-Aldrich, unless otherwise stated. Methacryloyl chloride (purum, dist., ≥97.0% GC), 11-bromo-1-undecanol (purum, ≥99.0%, AT), triethylamine (≥99.0%), diethyl chlorophosphate (97%), triethyl phosphite (98%), Aliquat 336 (Henkel), bromotrimethylsilane (purum, ≥97.0%), silica gel for chromatography (Merck KGaA, pore size 60 Å, mesh 0.2–0.5 mm), dichloromethane (≥99.8%), acetonitrile (≥ 99.9%), methanol (≥99.9%), ethyl acetate (≥99.8%), *n*-hexane (≥97.0%), sodium bisulfate (anhydrous, purum, ≈95.0%), sodium hydrogencarbonate (99.0%), sodium chloride (≥99.5%), 2,2′-azobis(2-methylbutyronitrile) (purum ≥98.0%), hexadecane (≥99.0%), potassium peroxodisulfate (KPS, puriss. p.a., ≥99.0%), cerium(III) nitrate hexahydrate (puriss. p.a., ≥99.0%), iron(III) chloride hexahydrate (puriss. p.a., ≥99%), iron(II) sulfate heptahydrate (≥99.0%), iron(III) nitrate nonahydrate (≥99.999%, trace metals basis), zinc acetate dehydrate (puriss. p.a., ≥99.0%), sodium hydroxide (≥97.0%), potassium hydroxide (≥85%), 2-propanol (99.9%), and rhodamine B (Sigma Aldrich, 97%) were used without further purification. Styrene (≥99.0%) was passed over an aluminum oxide column before use to remove the stabilizer.

Synthesis of 11-Bromoundecyl Methacrylate (**1**): 11-bromo-1-undecanol (5.0 g, 19.9 mmol) and triethylamine (4.18 mL, 3.04 g, 29.1 mmol, 1.5 eq) were dissolved in CH_2Cl_2 (50 mL) and the mixture was cooled to 0 °C. Subsequently, methacryloyl chloride (2.93 mL, 3.14 g, 30.0 mmol, 1.5 eq) was added dropwise over 30 min to the mixture. The mixture was allowed to warm to 25 °C and stirred for 12 h. After elimination of the solvents by rotoevaporation, the product was dissolved in ethyl acetate and filtrated to remove solid crystals of triethylammonium chloride. The organic phase was washed three times with 1 M solutions of sodium bisulfate, sodium hydrogencarbonate, and sodium chloride. The organic phase was dried over $MgSO_4$ and the solvent was removed in vacuum by rotoevaporation (maximum temperature: 35 °C). The crude yellowish product was purified by column chromatography (dichloromethane/*n*-hexane; 1:1; RF 0.6), resulting in a colorless oil (4.69 g, 14.7 mmol, 74% yield). ^{1}H NMR (300 MHz, $CDCl_3$, δ/ ppm): 6.31–5.98 (m, 1H), 5.74–5.43 (m, 1H), 4.13 (t, *J* = 6.7 Hz, 2H), 3.47 (dt, *J* = 37.2, 6.8 Hz, 2H), 2.04–1.92 (m, 3H), 1.94–1.77 (m, 2H), 1.77–1.62 (m, 2H), 1.50–1.22 (m, 14H). ^{13}C NMR (75 MHz, $CDCl_3$, δ/ ppm): 167.69, 136.72, 125.24, 64.95, 34.14, 32.97, 29.58, 29.55, 29.52, 29.35, 28.88, 28.74, 28.30, 26.10, 18.46.

Synthesis of 11-(Diethoxyphosphoryl)undecyl Methacrylate (**2**): In an argon atmosphere, compound **1** (2 g, 9.12 mmol, 1 eq) was dissolved in neat triethyl phosphite (8.60 mL, 8.34 g, 50.2 mmol, 5.5 eq) and refluxed at 140 °C for 12 h. The excess of triethyl phosphite was removed in vacuo and the crude product was purified by column chromatography (ethyl acetate, RF: 0.4). A colorless oil was obtained (2.98 g, 7.93 mmol, 87% yield). ^{1}H NMR (300 MHz, $CDCl_3$, δ/ ppm): 6.09 (s, 1H), 5.54 (s, 1H), 4.20–3.99 (m, 6H), 1.94 (s, 3H), 1.80–1.49 (m, 6H), 1.30 (m, 20H).). ^{13}C NMR (75 MHz, $CDCl_3$, δ/ ppm): 167.43, 137.22, 125.14, 64.85, 61.98, 61.88, 35.84, 32.97, 29.58, 29.67, 29.62, 29.45, 28.86, 28.71, 28.19, 26.03, 18.44, 16.42, 16.32. ^{31}P NMR (121 MHz, $CDCl_3$, δ/ ppm): 33.16.

Synthesis of (11-(Methacryloyloxy)undecyl)phosphonic Acid (**3**, RPO_3H_2): Under an argon atmosphere, compound **2** (2 g, 5.31 mmol) was dissolved in CH_2Cl_2 (10 mL) in a heated Schlenk tube, and bromotrimethylsilane (3.45 mL, 4.00 g, 26.1 mmol, 8 eq) was added dropwise to the solution. The reaction mixture was stirred for 12 h. Subsequently, 10 mL of methanol were added and the solution was stirred for another 1.5 h. After evaporation of the solvents, the surfmer was obtained as a colorless solid (quantitative reaction, 100% yield). ^{1}H NMR (300 MHz, MeOD, δ/ ppm): 6.00 (s, 1H), 5.53 (s, 1H), 4.06 (t, *J* = 6.6 Hz, 2H), 1.85 (s, 3H), 1.71–1.45 (m, 6H), 1.37–1.21 (m, 14H). ^{13}C NMR (75 MHz, MeOD, δ/ ppm): 167.62, 136.72, 125.24, 64.82, 34.02, 32.56, 29.54, 29.51, 29.48, 29.29, 28.83, 28.69, 28.27, 25.98, 18.21. ^{31}P NMR (121 MHz, MeOD, δ/ ppm): 37.16. FT-IR (KBr, υ/ cm^{-1}): 2924 (w), 2851 (w), 1716 (s), 1637 (m), 1470 (s), 1411 (vw), 1327 (vw), 1297 (vw), 1186 (m), 1106(w), 1053 (w), 1010 (w), 988 (m), 793 (m), 815 (m), 793 (m), 719 (s), 654 (vw), 604 (vw), 537 (s), 478 (m), 443 (vw), 419 (w). MALDI-TOF (*M* = 320.36 g mol^{-1}; *m*/*z* [*M*+]): 343 [+Na]$^+$, 321 [+H]$^+$, 274 [$-(CH_2 = C-(CH_3)-C = O)$ + Na]$^+$, 235 [$-(CH_2 = C-(CH_3)-COOH)$ + H]$^+$.

Synthesis of 11-Bromoundecyl Diethyl Phosphate (**4**): Under an argon atmosphere, 11-bromo-1-undecanol (5 g, 19.9 mmol) and triethylamine (8.36 mL, 6.08 g, 60.1 mmol, 3 eq) were dissolved in CH_2Cl_2 (50 mL) and the mixture was cooled to 0 °C. Subsequently, diethyl chlorophosphate (8.67 mL, 10.35 g, 60.1 mmol, 3 eq) was added dropwise over 30 min to the mixture. The mixture was allowed to warm to 25 °C and stirred for 48 h. The solvents were removed by rotoevaporation. The product was dissolved in diethyl ether and the solid crystals of triethylammonium chloride were removed by filtration. The organic phase was washed three times with a 1 M sodium chloride solution, dried over $MgSO_4$, and concentrated in vacuum (rotoevaporation at a max. temp. of 35 °C). The mixture was distilled in high vacuum to remove the excess of diethyl chlorophosphate, resulting in a yellow oil. The crude product was purified by column chromatography (EtOAc/*n*-hexane; 1:1; RF 0.4, TC stained with I_2), resulting in a slightly yellowish oil (4.82 g, 12.4 mmol, 62% yield). ^{1}H NMR (300 MHz, $CDCl_3$, δ/ ppm): 4.19–3.94 (m, 6H), 3.46 (dt, *J* = 37.2, 6.8 Hz, 2H), 1.92–1.59 (m, 4H), 1.48–1.18 (m, 20H). ^{13}C NMR (75 MHz, $CDCl_3$, δ/ ppm): 67.79, 63.66, 34.08, 32.80, 30.30, 29.50, 29.47, 29.45, 28.93, 28.80, 28.22, 26.93, 16.22. ^{31}P NMR (121 MHz, $CDCl_3$, δ/ ppm): –0.32.

Synthesis of 11-((Diethoxyphosphoryl)oxy)undecyl Methacrylate (**5**): Under an argon atmosphere, potassium methacrylate (2.04 g, 16.5 mmol, 1.5 eq) and compound **4** (4.25 g, 11.0 mmol) were dissolved in acetonitrile (47.1 g, 1.15 mol). Hydroquinone monomethylether (14 mg) was used for the stabilization of the methacrylate. Tricaprylmethylammonium chloride (Aliquat 336) was used as a phase transfer catalyst (2.5 g, 5 wt.%) and the mixture was refluxed for 24 h. Afterwards, the mixture was filtered and the solvent was removed by rotoevaporation. The residue was dissolved in $CHCl_3$ and washed three times with water. The organic phase was dried over $MgSO_4$ and concentrated under reduced pressure. The crude product was purified by column chromatography (EtOAc/*n*-hexane; 1:1; RF 0.4, TC stained with I_2), yielding a colorless liquid (2.76 g, 7.04 mmol, 64% yield). ^{1}H NMR (300 MHz, $CDCl_3$, δ/ ppm): 6.07 (s, 1H), 5.52 (s, 1H), 4.18–3.91 (m, 8H), 1.91 (s, 3H), 1.73–1.55 (m, 4H), 1.36–1.21 (m, 20H). ^{13}C NMR (75 MHz, MeOD, δ/ ppm): 168.36, 137.54, 125.40, 65.84, 34.22, 33.79, 30.74, 30.70, 30.46, 29.80, 29.63, 29.15, 27.24, 18.56, 16.29. ^{31}P NMR (121 MHz, $CDCl_3\delta$/ ppm): –0.37.

Synthesis of 11-(Phosphonooxy)undecyl Methacrylate (**6**, RPO_4H_2): Compound **5** (1.5 g, 3.82 mmol) and ethyl acetate (53 mg, 0.60 mmol) were dissolved in 10 mL CH_2Cl_2 (heated Schlenk tube) and bromotrimethylsilane (1.01 mL, 1.17 g, 7.64 mmol, 2 eq) was added dropwise to the solution. The ethyl acetate was used to avoid the cleavage of the long alkyl chain (surfmer spacer) and the phosphate group. The reaction mixture was stirred for 12 h. Subsequently, 10 mL of methanol were added and the solution was stirred for another 1.5 h. After evaporation of the solvents, a colorless viscous oil was obtained (99% yield). ^{1}H NMR (300 MHz, $CDCl_3$, δ/ ppm): 5.93 (s, 1H), 5.46 (s, 1H), 3.99 (t, *J* = 6.6 Hz, 2H), 3.28 (t, *J* = 6.7 Hz, 2H), 1.78 (s, 9H), 1.75–1.46 (m, 4H), 1.33–1.13 (m, 14H). ^{13}C NMR (75 MHz, MeOD, δ/ ppm): 168.86, 137.87, 125.92, 65.90, 34.41, 33.98, 30.55, 30.51, 30.29, 29.82, 29.67, 29.15, 27.05, 18.43. ^{31}P NMR (121 MHz, $CDCl_3\delta$/ ppm): –49.79. FT-IR (liquid, υ/ cm^{-1}): 2927 (m), 2853 (m), 1719 (s), 1637 (m), 1463 (s), 1403 (vw), 1375 (vw), 1321 (w), 1297 (m), 1170 (vs), 1033 (vs), 816 (w), 766 (vw), 725 (vw), 648 (m), 491 (s). MALDI-TOF (*M* = 336,36 g mol^{-1}, *m*/*z* [*M*+]): 359 [+Na]$^+$, 337 [+H]$^+$, 252 [$-(CH_2 = C-(CH_3)-COOH)$ + H]$^+$.

Synthesis of Phosphonate- and Phosphate-Functionalized Latex Particles: The latex particles were prepared by miniemulsion polymerization from styrene and a small amount of the previously synthesized surfmers (RPO_3H_2 or RPO_4H_2), which served as comonomer and surfactant at the same time. The disperse phase was prepared by mixing styrene (3 g) with hexadecane (125 mg) and 2,2′-azobis(2-methylbutyronitrile) (60 mg). The continuous phase was prepared by dissolving RPO_3H_2 or RPO_4H_2 (30 mg) and a defined amount of a 1 M aqueous solution of NaOH, (RPO_3H_2: 218 μL, RPO_4H_2: 208 μL; equivalent to OH–groups) in water (18 mL). Both phases were mixed and stirred for 45 min. The emulsification was achieved by ultrasonication for 3 min (Branson Digital Sonifier 450-D; ½ inch tip, 90% intensity, pulse 10 s, pause 2 s) while cooling in an ice–water bath to avoid polymerization due to heating. The reaction occurred at 60 °C in a closed flask under constant stirring and was stopped after 12 h. The resulting dispersion was filtered and purified by centrifugation dialysis (Amicon Ultra centrifugal filter unit, 30 kDa, Millipore). The dispersions were analyzed by NMR spectroscopy with suppressed D_2O signal before and after centrifugation to ensure that small water soluble polymer chains or unpolymerized surfmer is removed (NMR spectra are presented in Figures S24–S25, Supporting Information).

Synthesis of Sulfate-Functionalized Latex Particles: Sulfate-functionalized particles were synthesized by surfactant-free miniemulsion polymerization. Styrene (6.0 g), hexadecane (250 mg) and water (23 g) were homogenized by ultrasonication for 3 min (90% intensity, pulse 60 s, pause 5 s), and the resulting dispersion was transferred to a pre-heated flask (72 °C). Subsequently, KPS (120 mg dissolved in 1mL of water) was added with a syringe to the reaction mixture. The dispersion was stirred at 1400 rpm for 12 h, keeping the temperature constant at 72 °C. The product was purified as previously indicated.

Crystallization Experiments: All experiments were conducted at 25 °C in a closed flask using a ratio of 5 mmol of metal salt per gram of latex particle, which was found to show the best results in initial screening tests. Milli-Q water was used for all aqueous solutions and washing steps. All precursor solutions were freshly prepared to avoid altering and unwanted oxide formation during time. After crystallization, hybrid particles were purified by three steps of centrifugation and redispersion in the corresponding solvent and used for further investigations. The washed particles were centrifuged and dried under vacuum (48 h at 30 °C) for XRD, BET and VSM measurements.

Formation of Ceria at the Surface of Latex Particles: Cerium(III) nitrate hexahydrate was dissolved in 2 mL of water and 200 µL of the latex dispersion were added to the solution. The mixture was stirred for 1 h at 250 rpm for pre-complexation of the cerium ions. The precipitation of the oxide was induced by adding dropwise 2 mL of a NaOH aqueous solution (0.1 M) with a syringe pump (dropping speed of 1 mL h^{-1}). After the base addition, the mixture was stirred for 24 h to complete oxide formation.

Formation of Iron Oxide (Fe_2O_3 or Fe_3O_4) at the Surface of Latex Particles: Iron(III) chloride hexahydrate (for Fe_2O_3) or iron(II) sulfate heptahydrate (for Fe_3O_4) were dissolved in 2 mL H_2O and 200 µL of functionalized particle dispersion were added. The mixture was stirred at 250 rpm for 4 h. Subsequently, 1 mL of concentrated ammonia was added with the help of a syringe pump (dropping speed of 3 mL h^{-1}). For the formation of Fe_2O_3 at the surface of functionalized particles from 2-propanol, iron(III) nitrate nonahydrate was dissolved in 2-propanol (4 mL) and 200 µL of latex dispersion were added. The mixtures were additionally stirred for 24 h.

Formation of Zinc Oxide at the Surface of Latex Particles: Zinc acetate dihydrate was dissolved in 4 mL of an alcohol (methanol, ethanol or 2-propanol) and stirred for 2h to assure complete solution of the precursor. Subsequently, 100 µL of the dispersion were added and the mixture was stirred for another 2 h. Afterwards, 1 mL of a KOH alcoholic solution (0.1 M) was added with a syringe pump (dropping speed of 2 mL h^{-1}). The experiments from aqueous solution, which did not yield zinc oxide, were prepared analogously to those of ceria, but using zinc acetate dihydrate as a precursor.

Complexation Efficiency of Metal Oxide Precursor: To determine the complexation efficiency of the phosphonate- and phosphate-functionalized particles, 200 µL of the particle dispersion were added to 10 mL of the metal precursor solution (10 g L^{-1}). The mixtures were stirred as long as the complexation times indicated in the crystallization experiments. Afterwards, the collapsed dispersion was centrifuged, and the supernatant was investigated by ICP–OES.

Photocatalytic Degradation of Rhodamine B Supported by Ceria Hybrid Particles: An aqueous solution of rhodamine B (1 µg mL^{-1}) containing ceria hybrid particles (1 wt%) was stirred under UV light irradiation (mercury vapor lamp, UV-Consulting Peschl TQ 150, cooled in a water circulation system). For comparison of the catalytic activity the previous experiment was conducted with commercial CeO_2 powder (1 wt%) instead of hybrid. A blank sample without ceria hybrid particles was prepared with the same rhodamine B concentration and analogously treated. The degradation of the dye was followed by measuring the fluorescence emission of aliquots taken at different times.

Characterization Methods:^{1}H NMR, ^{13}C NMR and ^{31}P NMR spectra were recorded on a Bruker DRX spectrometer (300 MHz) at 298.3 K. The proton and carbon spectra were referenced using the remaining solvents signals as an internal standard (used solvents are shown in the corresponding signal lists). The signal of phosphoric acid was used as standard for the phosphor spectra. Fourier transform infrared (FTIR) spectra were registered in a Perkin Elmer Spectrum BX spectrometer. MALDI-TOF analysis was carried out with a Ultraflex Bruker Daltonics spectrometer using dithranol as carrying matrix.

Particle sizes of the prepared particles was determined by dynamic light scattering using a Nicomp particle sizer (model 380, PSS, Santa Barbara, CA) at a fixed angle of 90°. The solid content was determined by freeze-drying a portion of the dispersion under vacuum for 24 h. The surface-charge density was estimated as previously reported[66] by titration with a poly(diallyldimethylammonium chloride) solution (0.001 N, Mütek Analytik, M = 40 000–100 000 g mol^{-1}) utilizing a 702SM Titrino (Metrohm AG, Switzerland) automatic titrator (see Supporting Information for details).

The zeta potential of the functionalized latexes was determined by electrophoretic mobility measurements in a Malvern ZetaSizer Nano-Z instrument. For the measurements, the dispersions were diluted 1:1000 with a KCl solution (0.001 M) to achieve optical transparency for the measurements and shear off all diffuse adsorbed ion layers. The measurements were conducted three times per sample to proof the repeatability.

Scanning electron microscopy (SEM) was conducted in a field-emission microscope Leo Gemini 1530 operated with an extractor voltage of 0.7 kV. Samples for SEM observation were prepared by drop-casting of diluted dispersions on silicon wafers. Transmission electron microscopy (TEM), electron diffraction and energy-dispersive X-ray spectroscopy (EDX) were carried out in FEI Tecnai F20 microscope. EDX analysis combined with element mapping was carried out in a Hitachi SU8000 SEM microscope equipped with a Bruker AXS spectrometer with an operation voltage of 5 kV.

X-ray diffraction of the washed and vacuum dried samples was conducted on a Philips PW 1820 diffractometer with monochromatic $Cu_{K\alpha}$ radiation (λ = 1.5418 Å, 40 kV, 30 mA, 5 s, $\Delta\theta$ = 0.02). The estimation of crystallite sizes and the error calculations are described in the Supporting Information. X-ray diffraction of the calcinated samples (residue of the TGA analysis) were obtained in transmission on a Huber (image plate Guinier camera G670) diffractometer with $Cu_{K\alpha}$ radiation after fixing the powders in a polymer film (Mylar X-ray film).

Thermogravimetric analysis (TGA) was carried out with a thermobalance Mettler Toledo ThermoSTAR TGA/SDTA 851 under a nitrogen atmosphere (from 25 to 1000 °C with a heating rate of 10 °C min^{-1}).

Specific surface area was determined by measuring the nitrogen adsorption on an Autosorb MP1 instrument (Quantachrome). The surface area was calculated utilizing the five-point method according to the Brunauer–Emmett–Teller (BET) concept in the range of p/p_0 0.05–0.3. Before BET measurements, the dried hybrid particles were degassed at 60 °C for 48 h under vacuum to ensure the complete removal of any adsorbed material. Inductively coupled plasma–optical emission spectrometry (ICP–OES) was carried out on Activa simultaneous CCD–ICP–OES spectrometer (Horiba Jobin Yvon) by measuring aliquots of the analyte solution and correlating with reference measurements of the analyte. Each aliquot was measured three times and the average was used for calculations.

Photoluminescence (PL) emission and excitation spectra were recorded in top-reading mode in a Tecan Infinite M100 plate reader by using a quartz plate (Hellma Analytics).

Magnetic measurements were performed in a squid magnetometer (Quantum Design MPMS II). The weighted sample was filled in gelatine capsules and mounted in a low magnetic moment sample holder. The temperature sweeps were measured with a rate of 2 K min^{-1}. The hysteresis curves were measured with the magnet in the superconducting state at each field value. The SQUID signals resembled closely the expected signal from point dipoles and were calibrated against a Pd reference sample. Additional hysteresis measurements in a vibrating sample magnetometer (VSM) for some samples yielded identical results.

Supporting Information

Supporting Information is available from the Wiley Online Library or from the author.

Acknowledgements

The authors thank M. Steiert for XRD and ICP–OES measurements, B. Freisinger, and K. Kirchhoff for the assistance with some electron microscopy measurements, G. Glaßer for the EDX analysis, E. Muth for the help with the polyelectrolyte titration, and P. Kindervater for NMR measurements.

Received: July 4, 2012

---

[1] J. P. Chen, S. Patil, S. Seal, J. F. McGinnis, *Nat. Nanotechnol.* **2006**, *1*, 142–150.

[2] N. H. Cho, T. C. Cheong, J. H. Min, J. H. Wu, S. J. Lee, D. Kim, J. S. Yang, S. Kim, Y. K. Kim, S. Y. Seong, *Nat. Nanotechnol.* **2011**, *6*, 675–682.

[3] M. J. Jin, D. H. Lee, *Angew. Chem. Int. Ed.* **2010**, *49*, 1119–1122.

[4] C. Gonzato, M. Courty, P. Pasetto, K. Haupt, *Adv. Funct. Mater.* **2011**, *21*, 3947–3953.

[5] E. Redel, P. Mirtchev, C. Huai, S. Petrov, G. A. Ozin, *ACS Nano* **2011**, *5*, 2861–2869.

[6] E. J. Henderson, A. J. Shuhendler, P. Prasad, V. Baumann, F. Maier-Flaig, D. O. Faulkner, U. Lemmer, X. Y. Wu, G. A. Ozin, *Small* **2011**, *7*, 2507–2516.

[7] S. Muhlig, A. Cunningham, S. Scheeler, C. Pacholski, T. Burgi, C. Rockstuhl, F. Lederer, *ACS Nano* **2011**, *5*, 6586–6592.

[8] R. L. Liu, D. Q. Wu, S. H. Liu, K. Koynov, W. Knoll, Q. Li, *Angew. Chem. Int. Ed.* **2009**, *48*, 4598–4601.

[9] A. Khanal, Y. Inoue, M. Yada, K. Nakashima, *J. Am. Chem. Soc.* **2007**, *129*, 1534–1535.

[10] W. R. Zhao, J. L. Gu, L. X. Zhang, H. R. Chen, J. L. Shi, *J. Am. Chem. Soc.* **2005**, *127*, 8916–8917.

[11] T. Chen, P. J. Colver, S. A. F. Bon, *Adv. Mater.* **2007**, *19*, 2286–2289.

[12] H. M. Xiong, Y. Xu, O. G. Ren, Y. Y. Xia, *J. Am. Chem. Soc.* **2008**, *130*, 7522–7523.

[13] G. L. Athens, R. M. Shayib, B. F. Chmelka, *Curr. Opin. Colloid Interface Sci.* **2009**, *14*, 281–292.

[14] S. Neyshtadt, J. P. Jahnke, R. J. Messinger, A. Rawal, T. S. Peretz, D. Huppert, B. F. Chmelka, G. L. Frey, *J. Am. Chem. Soc.* **2011**, *133*, 10119–10133.

[15] E. Kang, H. Jung, J. G. Park, S. Kwon, J. Shim, H. Sai, U. Wiesner, J. K. Kim, J. Lee, *ACS Nano* **2011**, *5*, 1018–1025.

[16] M. Urban, A. Musyanovych, K. Landfester, *Macromol. Chem. Phys.* **2009**, *210*, 961–970.

[17] M. Agrawal, S. Gupta, A. Pich, N. E. Zafeiropoulos, M. Stamm, *Chem. Mater.* **2009**, *21*, 5343–5348.

[18] M. M. Titirici, M. Antonietti, A. Thomas, *Chem. Mater.* **2006**, *18*, 3808–3812.

[19] R. M. Erb, H. S. Son, B. Samanta, V. M. Rotello, B. B. Yellen, *Nature* **2009**, *457*, 999–1002.

[20] A. Navrotsky, C. C. Ma, K. Lilova, N. Birkner, *Science* **2010**, *330*, 199–201.

[21] D. Amara, J. Grinblat, S. Margel, *J. Mater. Chem.* **2010**, *20*, 1899–1906.

[22] B. Perlstein, T. Lublin-Tennenbaum, I. Marom, S. Margel, *J. Biomed. Mater. Res. Part B* **2010**, *92B*, 353–360.

[23] J. Qin, S. Laurent, Y. S. Jo, A. Roch, M. Mikhaylova, Z. M. Bhujwalla, R. N. Muller, M. Muhammed, *Adv. Mater.* **2007**, *19*, 1874–1878.

[24] K. Katagiri, Y. Imai, K. Koumoto, T. Kaiden, K. Kono, S. Aoshima, *Small* **2011**, *7*, 1683–1689.

[25] M. Liong, J. Lu, M. Kovochich, T. Xia, S. G. Ruehm, A. E. Nel, F. Tamanoi, J. I. Zink, *ACS Nano* **2008**, *2*, 889–896.

[26] M. Yoon, Y. Kim, J. Cho, *ACS Nano* **2011**, *5*, 5417–5426.

[27] Y. R. Lin, G. Ehlert, H. A. Sodano, *Adv. Funct. Mater.* **2009**, *19*, 2654–2660.

[28] P. X. Gao, Y. Ding, W. J. Mai, W. L. Hughes, C. S. Lao, Z. L. Wang, *Science* **2005**, *309*, 1700–1704.

[29] Z. L. Wang, J. H. Song, *Science* **2006**, *312*, 242–246.

[30] A. B. Djurisic, W. C. H. Choy, V. A. L. Roy, Y. H. Leung, C. Y. Kwong, K. W. Cheah, T. K. G. Rao, W. K. Chan, H. T. Lui, C. Surya, *Adv. Funct. Mater.* **2004**, *14*, 856–864.

[31] R. O. Moussodia, L. Balan, C. Merlin, C. Mustin, R. Schneider, *J. Mater. Chem.* **2010**, *20*, 1147–1155.

[32] Y. S. Fu, X. W. Du, S. A. Kulinich, J. S. Qiu, W. J. Qin, R. Li, J. Sun, J. Liu, *J. Am. Chem. Soc.* **2007**, *129*, 16029–16033.

[33] L. Qi, A. Sehgal, J. C. Castaing, J. P. Chapel, J. Fresnais, J. F. Berret, F. Cousin, *ACS Nano* **2008**, *2*, 879–888.

[34] A. B. Kehoe, D. O. Scanlon, G. W. Watson, *Chem. Mater.* **2011**, *23*, 4464–4468.

[35] H. Tamai, H. Yasuda, *J. Colloid Interface Sci.* **1999**, *212*, 585–588.

[36] A. Ethirajan, K. Landfester, *Chem. Eur. J.* **2010**, *16*, 9398–9412.

[37] S. Schachschal, A. Pich, H. J. Adler, *Colloid Polym. Sci.* **2007**, *285*, 1175–1180.

[38] Y. Lu, Y. Mei, M. Drechsler, M. Ballauff, *Angew. Chem. Int. Ed.* **2006**, *45*, 813–816.

[39] Y. Mei, Y. Lu, F. Polzer, M. Ballauff, M. Drechsler, *Chem. Mater.* **2007**, *19*, 1062–1069.

[40] M. Schrinner, M. Ballauff, Y. Talmon, Y. Kauffmann, J. Thun, M. Moller, J. Breu, *Science* **2009**, *323*, 617–620.

[41] M. Agrawal, A. Pich, N. E. Zafeiropoulos, S. Gupta, J. Pionteck, F. Simon, M. Stamm, *Chem. Mater.* **2007**, *19*, 1845–1852.

[42] M. Agrawal, S. Gupta, A. Pich, N. E. Zafeiropoulos, J. Rubio-Retama, D. Jehnichen, M. Stamm, *Langmuir* **2010**, *26*, 17649–17655.

[43] M. Agrawal, A. Pich, S. Gupta, N. E. Zafeiropoulos, P. Simon, M. Stamm, *Langmuir* **2008**, *24*, 1013–1018.

[44] M. Agrawal, A. Pich, S. Gupta, N. E. Zafeiropoulos, P. Formanek, D. Jehnichen, M. Stamm, *Langmuir* **2010**, *26*, 526–532.

[45] Y. Lu, M. Hoffmann, R. S. Yelamanchili, A. Terrenoire, M. Schrinner, M. Drechsler, M. W. Moller, J. Breu, M. Ballauff, *Macromol. Chem. Phys.* **2009**, *210*, 377–386.

[46] Y. Lu, T. Lunkenbein, J. Preussner, S. Proch, J. Breu, R. Kempe, M. Ballauff, *Langmuir* **2010**, *26*, 4176–4183.

[47] R. Sauer, P. Froimowicz, K. Schöller, J.-M. Cramer, S. Ritz, V. Mailänder, K. Landfester, *Chem. Eur. J.* **2012**, *18*, 5201–5212.

[48] V. Fischer, K. Landfester, R. Muñoz-Espí, *Cryst. Growth Des.* **2011**, *11*, 1880–1890.

[49] A. F. Holleman, E. Wiberg, *Lehrbuch der Anorganischen Chemie*, 102 ed., De Gruyter, Berlin **2007**.

[50] J. Hartmann-Schreier, *RÖMPP Online – Version 3.21*, Georg Thieme Verlag, Stuttgart **2012**.

[51] M. Niederberger, *Acc. Chem. Res.* **2007**, *40*, 793–800.
[52] D. Gebauer, H. Cölfen, *Nano Today* **2011**, *6*, 564–584.
[53] D. Gebauer, A. Volkel, H. Cölfen, *Science* **2008**, *322*, 1819–1822.
[54] R. L. Rebodos, P. J. Vikesland, *Langmuir* **2010**, *26*, 16745–16753.
[55] X. Z. Wang, Z. B. Zhao, J. Y. Qu, Z. Y. Wang, J. S. Qiu, *Cryst. Growth Des.* **2010**, *10*, 2863–2869.
[56] H. Hecht, E. Mollwo, *Solid State Commun.* **1971**, *9*, 2167–2171.
[57] P. D. Yang, H. Q. Yan, S. Mao, R. Russo, J. Johnson, R. Saykally, N. Morris, J. Pham, R. R. He, H. J. Choi, *Adv. Funct. Mater.* **2002**, *12*, 323–331.
[58] R. Dingle, *Phys. Rev. Lett.* **1969**, *23*, 579–581.
[59] K. Vanheusden, W. L. Warren, C. H. Seager, D. R. Tallant, J. A. Voigt, B. E. Gnade, *J. Appl. Phys.* **1996**, *79*, 7983–7990.
[60] H. J. Egelhaaf, D. Oelkrug, *J. Cryst. Growth* **1996**, *161*, 190–194.
[61] E. G. Bylander, *J. Appl. Phys.* **1978**, *49*, 1188–1195.
[62] D. S. Bohle, C. J. Spina, *J. Am. Chem. Soc.* **2007**, *129*, 12380–12381.
[63] R. Muñoz-Espí, G. Jeschke, I. Lieberwirth, C. M. Gómez, G. Wegner, *J. Phys. Chem. B* **2007**, *111*, 697–707.
[64] S. Fujitsu, K. Koumoto, H. Yanagida, Y. Watanabe, H. Kawazoe, *Jpn. J. Appl. Phys. Part 1* **1999**, *38*, 1534–1538.
[65] H. Zhou, H. Alves, D. M. Hofmann, B. K. Meyer, G. Kaczmarczyk, A. Hoffmann, C. Thomsen, *Phys. Status Solidi B* **2002**, *229*, 825–828.
[66] R. Muñoz-Espí, Y. Qi, I. Lieberwirth, C. M. Gómez, G. Wegner, *Chem. Eur. J.* **2006**, *12*, 118–129.